Textile Research Journal

Original article

Textile Research Journal
2020, Vol. 90(1) 24–36

DOI: 10.1177/0040517519855316
journals.sagepub.com/home/trj
SAGE

Analyzing the effect of nanofiber orientation on membrane filtration properties with the progressive increase in its thickness: a numerical and experimental approach

Obed Akampumuza[1], Huilin Xu[1], Jian Xiong[1], Hongnan Zhang[1], Zhenzhen Quan[1,2] and Xiaohong Qin[1]

Abstract

One of the merits of modeling is that the computer-generated data is used in optimizing equipment and experimental designs, eliminating the costs associated with scaling up by experimentation. In this work, the filtration performance of nanofibers aligned diversely within virtual webs was numerically analyzed using Star CCM + and Ansys Fluent software. This knowledge was then used to fabricate two distinctly oriented nanofiber membranes via free surface electrospinning. Their filtration performance was studied by capillary flow porometry technology using POROLUX^{TM} 100. The results of this were in agreement with the simulation work.

Keywords

three-dimensional nanofiber virtual webs, fluid flow analysis, needleless electrospinning, capillary flow porometry

In designing a filter, a great deal of effort is committed to optimizing the fluid flow process through it, as during use, the nature of the flow determines the pressure drop experienced, which in turn impacts the filter feasibility. Whereas the flow varies from the microscopic to the macroscopic scale, the physics principles involved remain almost the same. The major structural unit of a filter is a fiber and this has been represented by a cylinder in most of the works pertaining to filtration. In the simplest model, flow against a sole cylinder has been considered.[1] In this highly porous domain of an infinitely long cylinder perpendicular to fluid flow, the effects of the neighboring fibers on that under consideration were neglected. Although Lamb[1] included inertia in his flow analysis, it was later revealed that Stokes equations of creeping flow govern the fluid motion within the porous medium, and that inertial effects remain negligible when compared with viscous effects throughout the entire region of flow.[2] Tamada and Fujikawa[3] showed that at low Reynolds number, the drag experienced by cylinders becomes directly proportional to the product of the viscosity coefficient (μ) and the undisturbed flow speed (U) to give a characteristic Stokes flow that relies on Darcy's law[4]

$$\langle u \rangle = -\frac{k}{\mu}\nabla p \tag{1}$$

Thus, the above model was then improved to a row of equidistant cylinders bearing the same diameter in which the effect of the neighboring fibers was well catered for. Miyagi[5], Kuwabara[6] and Happel[7] adopted

[1]Key Laboratory of Textile Science & Technology, Ministry of Education, College of Textiles, Donghua University, P. R. China
[2]The Innovation Center for Textiles Science and Technology, Donghua University, P. R. China

Corresponding authors:
Xiaohong Qin, Donghua University, 2999 Renmin Road, Songjiang, Shanghai 201620, P. R. China.
Email: xhqin@dhu.edu.cn
Zhenzhen Quan, Donghua University, 2999 Renmin Road, Songjiang, Shanghai 201620, P. R. China.
Email: quan@dhu.edu.cn

a cell model in which the filter was represented by a circular cell having a fiber in the center representing the solid volume fraction (SVF) of the filter. The influence of the neighboring fibers was accounted for using a microscopic envelope around the central fiber, with the characteristic envelope size depending on the macroscopic voids. Whereas the former assumed zero vorticity

$$\frac{\partial u_\theta}{\partial r} - \frac{1}{r}\frac{\partial u_r}{\partial \theta} - \frac{u_\theta}{r} = 0 \tag{2}$$

the latter considered zero tangential stress

$$\frac{\partial u_\theta}{\partial r} + \frac{1}{r}\frac{\partial u_r}{\partial \theta} - \frac{u_\theta}{r} = 0 \tag{3}$$

Practically, when a fluid flows from the downstream side of the filter to its upstream side, there will be a change in the original pressure, given by

$$\Delta P = P_1 - P_2 \tag{4}$$

Intrinsically, this drop results from the resistance to flow accrued as the fluid snakes its way through an intricate maze of pores created when fibers settle over each other during the membrane formation process. During flow, a considerable amount of fluid momentum will then be transferred to the fibers in the form of flow resisting drag.[8] This dimensionless fiber drag (F^*) has been derived as a function of the drag force (F) acting on a unit length of each cylinder/fiber, which is

$$F^* = F_f \mu U_0 \tag{5}$$

Accordingly, for relatively highly porous structures in which $\frac{r_f}{2h} \ll 1$ for two adjacent fibers with each having radius r_f and separated by a distance $2h$, different authors have provided varying formulations of F^* with the divergence in these attributed to the use of differing boundary conditions[9]

Davies[10]

$$F^* = 16\pi\alpha_f^{1/2}\left(1 + 56\alpha_f^3\right) \tag{6}$$

Happel[7]

$$F^* = 8\pi\frac{1}{-\ln\alpha_f - \left(1 - \alpha_f^2/1 + \alpha_f^2\right)} \tag{7}$$

Kuwabara[6]

$$F^* = 8\pi\frac{1}{-\ln\alpha_f + 2\alpha_f - 0.5\alpha_f^2 - 3/2} \tag{8}$$

Fuchs et al.[11]

$$F^* = 8\pi\frac{1}{-\ln\alpha_f - 3/2} \tag{9}$$

On the other hand, for densely packed membranes such that the size of the gap separating the two adjacent fibers is much smaller than the constituent cylinder radius, Keller[12] applied the lubrication theory to determine the drop in pressure

$$F^* = \frac{9\pi}{2\sqrt{2}}\left(1 - \frac{r_f}{h}\right) \tag{10}$$

Generally, drag relates to the pressure drop across the filter according to

$$\Delta P = F^* U_0 \mu \alpha_f Z / \pi a^2 \tag{11}$$

Virtual membrane fabrication has received a tremendous boost recently with the development of computing tools capable of conveniently generating three-dimensional (3D) webs having the physical properties of real filter membranes unto which the filter properties can be seamlessly analyzed. A number of authors have relied on this to characterize filter membrane permeability and performance and generally improve the filter properties.[13,14] Among others, Fraunhofer ITWM has developed a software platform GeoDict/FilterDict[15] that is capable of resolving the smallest scale of media while accounting for some of the crucial phenomena at this level, such as the slip flow and pore structure. In this work, 3D virtual webs were created in which the pore geometry was altered by controlling the fiber alignment. Computational fluid dynamics (CFD) was then used to analyze the extent to which this would affect the filter properties. The results of the simulation process were corroborated with those from the real aligned nanofiber and random fiber membranes fabricated on a needleless electrospinning machine. For these membranes, the effect of altering fiber alignment on porosity was studied using capillary flow porometry.

Numerical study

Geometry design

A fiber unit bears very close semblance to a cylinder; thus, cylinders have been used to geometrically represent fibers in most of the existing numerical and theoretical models. In addition, they have finite dimensions, which aid in the accurate representation of the actual fiber and filter media parameters, such as fiber length, diameter, filter packing density, thickness and SVF. In this work, 3D cylinders generated via a MATLAB code

were used to represent nanofibers. Fiber orientation being the backbone of our study, four different idealist designs were built, with all having fibers lying along the XY plane and transverse to air flow. The adopted designs were as follows. (i) Aligned fiber orientation where fibers in all the layers lie along the same direction in a 'close to' parallel arrangement (Figure 1(a)). In this, a very minor degree of deviation was introduced to replicate real-life aligned fiber webs where the fibers are not perfectly parallel. (ii) In orthogonal arrangement, Figure 1(b), fibers at each layer were almost unidirectional but the deposition direction was switched by 90 º at each successive step. (iii) Random fiber webs had fibers oriented at different angles from each other. In these, the randomness level differed a little for each of the structures (Figures 1(c) and (d)). In all the models, the filter volume was kept uniform (40 * 40 * t) μm^3 at each level (t representing the filter thickness) and, within this thickness, the total volume of the fibers was kept uniform at approximately 23%. This percentage was independent of the number of layers under consideration. The total fiber volume was determined from the expression

$$V_m = \pi r_f^2 (L_1 + L_2 + L_3 + \cdots + L_n) \qquad (12)$$

where V_m is the membrane volume, L is the length of the respective fibers, n is number of fibers in the membrane and r_f is the fiber radius.

Computational domain setup

The computational domain was built with the filter medium positioned right in the middle, then there was a provision for an air buffer 10 times (*10) for the unit fiber diameter on both the upstream and downstream sides of the media to facilitate in the smooth flow of air (Figure 1(e)). Fibers were prescribed as solid walls and the inlet and outlet as velocity and pressure boundaries, respectively, whereas the remaining sides were set to symmetry boundaries since no lateral flow of air was involved (Figure 1(e)). For the flow study, the commercial CFD package Star CCM + was used in the analysis. This boasts of a range of tools that are useful for this flow case, which among others offer the choice for slip flow at the nanofiber boundaries.

Slip flow physics, the meshing process and the general fluid flow process

Slip flow physics was adopted for the shear stress of air on the fiber surfaces. Air flow behavior around

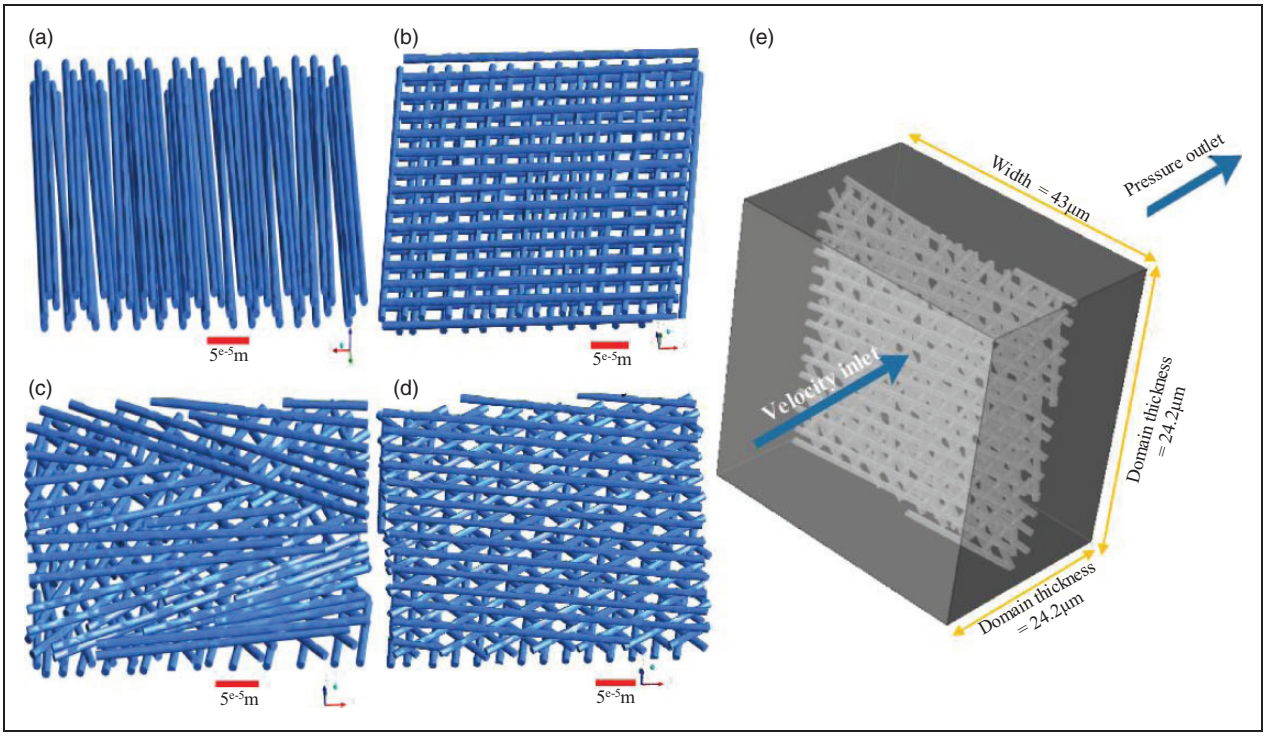

Figure 1. Fiber layout within virtual webs and the positioning of virtual webs within the computational domain: (a) parallel fiber array; (b) orthogonal layout; (c) controlled random fiber layout; (d) non-controlled random fiber layout; (e) the computational domain region showing the details of dimensions and major components (a velocity inlet, a pressure outlet and the symmetry sides).

cylindrical obstacles depends on the relative size of the cylinder diameter (d_f) and the distance traveled by gas molecules between successive collisions ($\lambda \approx 68$ nm at room temperature and ambient pressure), expressed in form of the Knudsen number K_n as

$$K_n = \frac{2\lambda}{d_f} \tag{13}$$

Guided by this relationship, the flow has been categorized into various regimes (Table 1).

For much larger objects (fibers) in the air flow path relative to the mean free path of air molecules, the mass averaged velocity of gas molecules momentarily comes to zero at their surfaces to give a continuum flow regime. On the other hand, as the fiber size reduces to within the proximity of the mean free path (typical electrospun nanofiber diameters), the majority of the air molecules will not have their velocities dropping to zero at the fiber surface but will somehow slip past it. In this regard, the 1 μm diameter cylinders used in this work fall under the slip flow category. Thus, a Maxwell[16] approach was adopted and an empirical slip coefficient [$C_s(K_n)$] was added to the continuum flow model[17]

$$u_s = \frac{2-\sigma_v}{\sigma_v} C_s(K_n)\lambda \left.\frac{\partial u}{\partial n}\right|_w = \Lambda \left.\frac{\partial u}{\partial n}\right|_w \tag{14}$$

where u_s is the slip velocity at the wall, σ_v is the tangential momentum accommodation coefficient and $\Lambda = [2-\sigma_v/\sigma_v]K_n C_s(K_n)$ is a non-dimensional form of the coefficient when the gradient at the wall is $[\partial u/\partial n]$.

The computational domain region was meshed with a *surface remesher* for a quality mesh on the domain surfaces, a *prism layer mesh* for the appropriate refinement of nanofiber surfaces and a *trimmer mesh* for the whole volume. These were applied concurrently. For the fluid flow analysis, the steady-state incompressible flow of air was studied using a segregated flow model to solve the governing equations

$$\nabla \cdot U_0 = 0 \tag{15}$$

$$\frac{\partial U_0}{\partial t} + u_0 \cdot \nabla U_0 = \nabla(p/\rho) + v\nabla \cdot \nabla U_0 \tag{16}$$

A segregated model solves the flow equations in an uncoupled manner.

Star-CCM + uses the finite volume discretization approach to sub-divide the solution domain into a finite number of small control volumes where each is subjected to a discrete integral form of the continuum transport equations to obtain linear algebraic equations. Here, the total number of unknowns in each equation corresponds to the number of cells in the grid that are solved by a multi grid solver. A comparison of the flow behavior in webs bearing different orientations was done starting from when each of the webs had only two layers until this number reached five. Thus, at each stage, four sets of simulations were done (one for each fiber orientation), a cycle that was repeated four times to cater for when the number of layers was three, four and five, respectively. However, for brevity, only a visual representation of the velocity profiles for four nanofiber layers is presented here (Figure 2). In all simulations, an inlet velocity of 0.1 m/s was used.

Media pressure drop and permeability

The formation of nanofiber membranes by needleless electrospinning involves the cumulative growth of fiber layers on each revolution of the cylindrical collector. The pattern and orientation of the fibers from this process can potentially affect the trend of pressure drop in these membranes. Thus, the pressure drop resulting from laying fibers differently within 3D virtual webs was analyzed as the number of nanofiber layers in the membrane grew. For convenience, at each level, the volume of fibers was kept uniform for all the orientations in consideration. Also, in all, the flow was in the transverse direction. Since pressure drop is a precursor to membrane permeability, the filter properties that define pressure drop will directly affect the permeability. Hence, for each of the different fiber arrangements, once the pressure drop across the webs had been established, permeability could then be calculated from Darcy's

Table 1. Knudsen numbers and their corresponding fluid flow regimes

Knudsen number (K_n)	The diameter of the fiber (d_f)	Flow regimes around fibers
$K_n < 0.001$	$d_f > 132\,\mu m$	Continuum flow
$0.001 < K_n < 0.25$	$528\,nm < d_f < 132\,\mu m$	Slip flow
$0.25 < K_n < 10$	$13.2\,nm < d_f < 528\,nm$	Transition flow
$K_n > 10$	$d_f < 13.2\,nm$	Free molecular flow

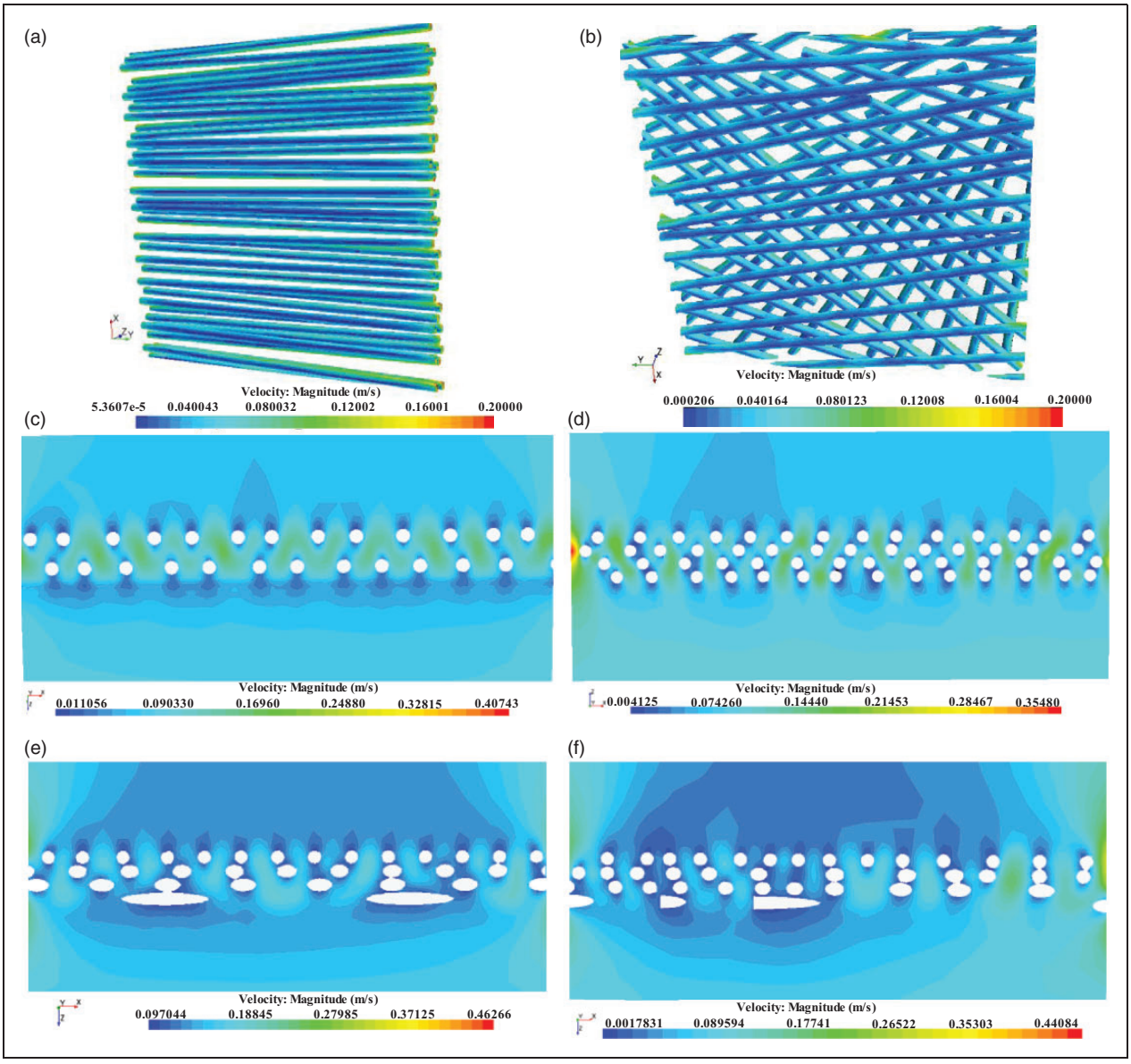

Figure 2. Cross-sections of the computational domains showing the velocity profiles for the flow of air through fiber membranes. The round structures are a two-dimensional representation of the nanofibers. It should be noted that except for the fiber orientation, other membrane physical properties were kept uniform, including fiber radius, total fiber volume and the number of fiber layers.

equation (Equation (1))

$$k(\,permeability) = \left| -\frac{u\mu}{\nabla p} \right| \tag{1}$$

The filtration performance of the filter webs and their respective figure of merit

Having obtained the velocity profiles of air flow through the webs, it becomes convenient to determine the particle trajectories since they flow along with fluid through the fiber network. Multiphysics software – Ansys Fluent – was used in the particle flow analysis. Meshing was done with an inbuilt mesher. In this CFD-Lagrangian study, appropriate settings were activated for both the particles and fibers to capture and record the resulting interactions. A clean filter approach was adopted in which particles were assumed not to clog the filter. Also, there was no particle–particle interaction in flight. Anthracite particles of 0.7 μm were used and, for CFD, a flow speed of 0.5 m/s was chosen for all simulation runs. For this size of particles, gravitational force was excluded. The major fluid force on the particles was considered to be the drag force, and physics for drag on the smooth spherical particles was activated. This drag

force acts as a mechanism by which a particle tries to catch up with the changing velocities of the surrounding fluid and this is generally expressed as

$$F_d = \frac{u_f - u_p}{\tau} \tag{17}$$

Here, u_f and u_p are the fluid and particle velocities, respectively, and in a Stokes drag regime, τ is given by

$$\tau = 2\rho_p^0 r^2 \Big/ 9\mu \tag{18}$$

The results of this process are presented in Figure 3(a), while Figure 3(b) gives the results of interactive relationship between the pressure drop of the filter and the particle capture efficiency, also known as quality factor or the figure of merit (FOM)

$$FOM = \frac{\ln(P_n)}{\Delta P} \tag{19}$$

Here, P_n is the penetration and ΔP is the pressure drop as the fluid goes through the filter. The results of this assessment are graphically presented in Figure 3(b). It has to be noted that efficiency, which is the reciprocal of penetration, is derived from the number of particles that are able to successfully go through the filter medium of those originally injected into the filter, given by the formula

$$E = \frac{N - N_0}{N_0} \tag{20}$$

Numerical study: discussions of the results

Fluid flow process (pressure drop and permeability). As the thickness of the membrane increases, pores will reduce in diameter, increasing the pressure drop through them. Here, we explore the relationship between the membrane pore evolution and permeability for different nanofiber orientations with the progressive growth of filter thickness. A closer look at the cross-section of aligned and orthogonally laid nanofiber webs shows an almost uniform distribution of pore sizes (Figures 2(a) and (b)). The pore size distribution was the least homogeneous in randomly laid structures. A reduction in the uniformity of flow distribution is generally accompanied by a reduction in the pressure drop. Flow through the gaps (pores) created between the fibers is normally in accordance with Bernoulli's principle, whereby the increased presence of larger gaps means lower flow velocities translating into reduced pressure drop. For this reason, only minimal pressure was experienced in membranes where the randomness was highest. From the graph of membrane permeability, with increasing thickness, Figure 4(b), a similar trend is observed in both the random and aligned webs, where the initial addition of an extra layer creates a miniature jump in the membrane permeability, after which the curves flatten with the addition of more layers. The fibers in the added layers did not cause a sufficient reduction in the sizes of the existing pores. On the other hand, with orthogonal and controlled random membranes, a balanced relationship between the increase in thickness and pressure drop was observed.

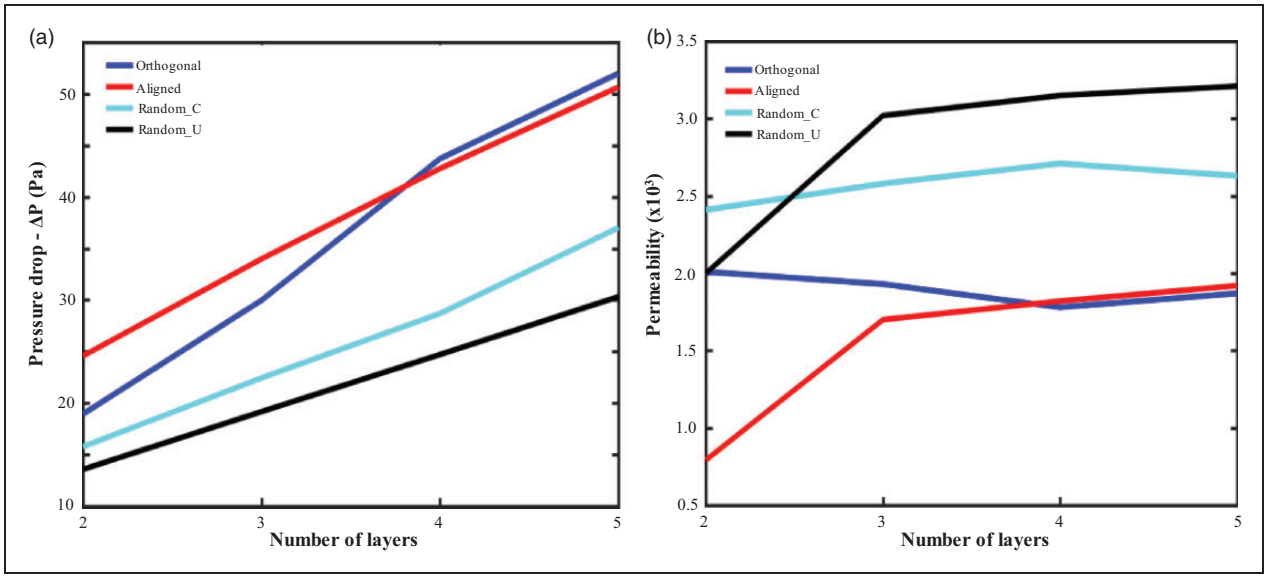

Figure 3. (a) Graph of the pressure drop within the membranes under consideration as the fiber layers are progressively increased. The inlet velocity was maintained at 0.1 m/s for all the models. Also, slip flow was considered at the fiber boundaries. (b) Graph of permeability corresponding to pressure drops in (a). Darcy's equation (Equation (1)) was used.

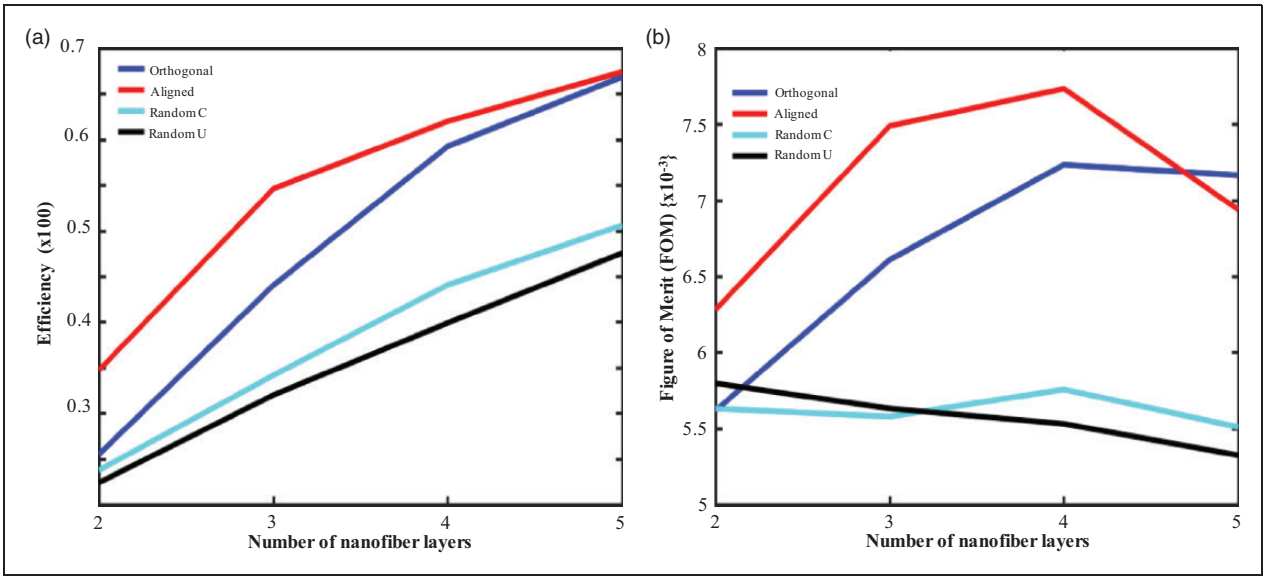

Figure 4. (a) The rise in efficiency as the number of nanofiber layers in the membrane are progressively increased. (b) Plots for the corresponding figure of merit.

Particle fiber interactions and the quality factor. As expected, there was a general uptrend in efficiency with the step-by-step addition of extra cylinder layers for all the models under consideration. Looking at the performance of individual models, the aligned webs gave the highest particle capture efficiency, while uncontrolled random webs gave the overall least efficiency. As air/fluid goes through a filter, it will tend to take the path where the openings are larger. A recipe for larger pores is that relatively fewer fibers are available in those particular positions of the membrane and, since the fluid acts a carrier for the particles, more particles too will be passing in places where there will be fewer obstacles (fibers/cylinders), presenting fewer chances of collision. This explains why in the random model, where the porous structure is most open, we get the least capture efficiency. In the filtration process, whereas maximizing efficiency is quite desirable, it can be accompanied by very high pressure that would in effect render the filter uncomfortable to use. The FOM is used assess the filter for a balance between pressure drop and efficiency. Whereas the aligned nanofiber membrane filters experienced the highest pressure drop, this was compensated for by equally high particle capture efficiency to still give it the highest quality factor.

Experimental details

Modeling eliminates the costs that would otherwise be incurred to do the scale up and optimization by experimentation, where the ideas obtained through the simulation process can be used to directly fabricate the final product. Since it was not practical to do a systematic process of studying the changes brought about by each extra layer experimentally, effort was made to replicate two of the major orientations dealt with in the simulation, namely random nanofiber membranes and relatively unidirectional fiber membranes.

Materials

Polyacrylonitrile (PAN) (Mw = 75,000) was purchased from Shanghai Chemical Fibers Institute. *N,N*-Dimethylformamide (DMF) was purchased from Shanghai Lingfeng Chemical Reagent Co., Ltd, China. Polypropylene (PP) nonwoven fabric with negligible filtration efficiency (1%) and pressure drop (4 Pa) under airflow velocity of 5.3 cm^{-1} was purchased from Nantong Yipinju Fabric Co., Ltd, China. All the chemical reagents were of analytical degree and used without further purification.

Random nanofiber and aligned nanofiber membrane fabrication process

PAN solution was prepared by dissolving PAN powder in DMF solution and mechanically stirring the two for 12 hours under ambient conditions. The alignment of nanofibers is a particularly meticulous process in which an optimum solution viscosity has to be maintained to enable jet stability. Also, a certain membrane withdrawal speed is necessary to align the fibers. To conform to these factors, 16% concentration was adopted for both aligned and random membranes. Also, to

achieve fiber alignment in one of the membranes, the collecting roller was set to rotate at a speed of 150 rpm. This speed was reduced to half (75 rpm) for the fabrication of random nanofiber membranes and the spinning time was the same for both. In both cases, a steady spinning rate was achieved at a voltage of 60 kV. The free surface electrospinning machine consisted of a ball spinneret connected to a long stick handle that was manually and gently turned around within a solution reservoir during the electrospinning process, a high-voltage power supply and a grounded rotating roller (Figure 5(a)). The ball was charged with high voltage and, once rolled around within the solution, the jets would spring off its surface. This spinning mechanism is not custom tailored for making aligned membranes and due modifications had to be done on its motor to achieve the speeds required for the aligned deposition.

Analysis

Micrography. The nanofiber web morphology was observed using a KYKY EM6200 scanning electron microscope (Figure 6).

Porometry. The POROLUX^{TM} 100 uses a pressure scan method in which a single valve is opened during measurement; the pressure and the resulting gas flow are then measured continuously. In this experiment, data for the pressure versus flow rate of nitrogen gas through dry samples taken from both membranes was used in generating the plots given in Figure 7. Membrane samples were then wetted, after which nitrogen gas was run through them to displace the wetting liquid. The POROLUX works on the principle that the liquid in the largest pore is displaced (blown out) first, while that in the smallest pore comes out last. These liquid flow rates are measured using a built-in liquid flow meter or microbalance. The differential filter flow gives the data for the amount of flow corresponding with the available pore sizes. This flow data for random and aligned nanofiber membranes is given in Figures 7(c) and (d), respectively.

The significance of steadily increasing the flow rate through the membrane on the membrane properties. Having analyzed the flow through electrospun membranes with increasing fluid flow rates versus the accrued pressure drop using the POROLUX equipment, Figure 7(a), an extra effort was undertaken to establish the kind of performance that would be exhibited by the 3D virtual membranes if subjected to progressively increasing airflow rates (that is, different inlet velocities). Thus, for each of the fiber alignments under consideration, the membrane of five layers was chosen to represent the remaining layers, and each of these was consequently subjected to airflow velocities of 0.1, 0.3, 0.5, 0.7 and 1 m/s. Both Ansys and Star CCM + CFD softwares were used in this study. The data generated in this study is presented in graphs in Figure 8(b). It should be noted that whereas the POROLUX filter

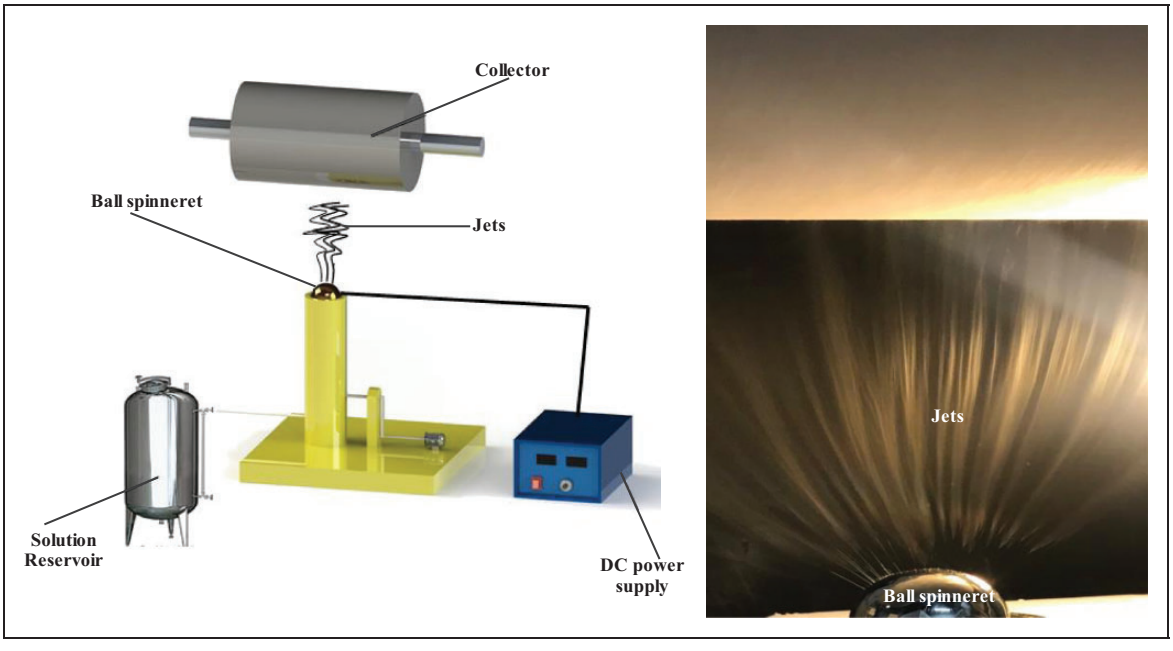

Figure 5. (a) Schematic of the free surface electrospinning setup consisting of high throughput ball electrospinning. (b) Still image of the jets coming off a charged ball spinneret. DC: direct current.

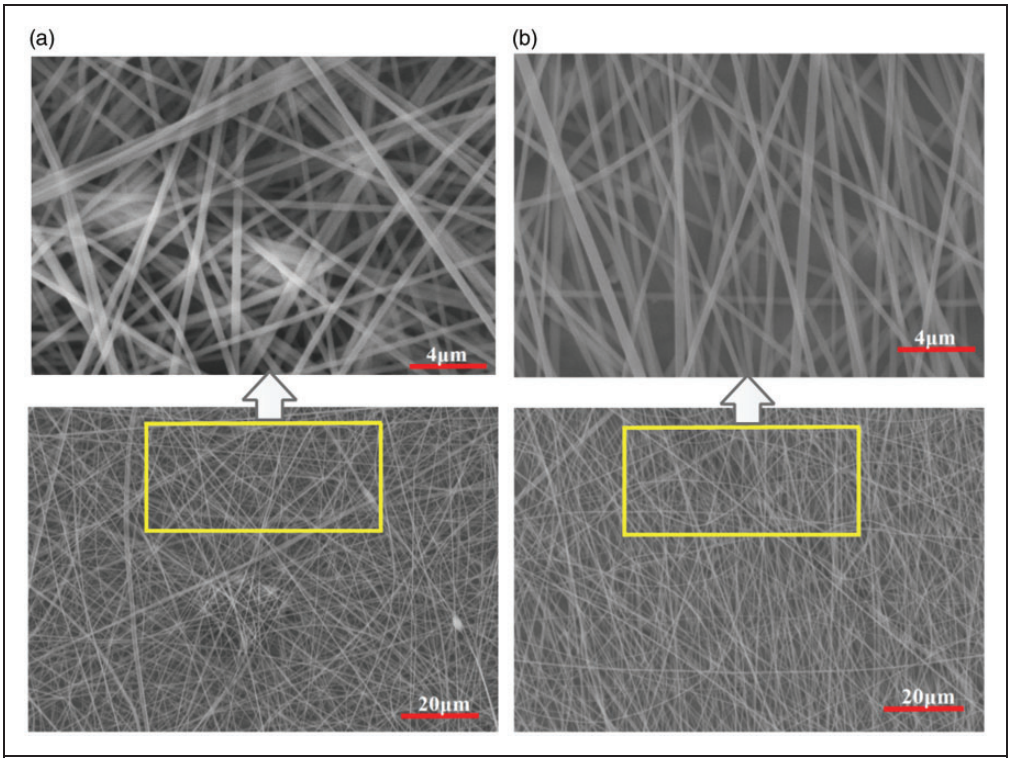

Figure 6. Scanning electron microscopy images of (a) random nanofiber membranes and (b) relatively aligned nanofiber membranes prepared by needleless electrospinning using a ball spinneret.

membrane testing machine accurately predicts the trend between the fluid flow rate and pressure drop, the given pressure drop values may not be quite realistic; this is often due to the initial pressure settings and the very small sample size used. For this reason, an automatic filtration testing unit (Model 8130, TSI Group, USA) was used to corroborate the results; the data obtained corresponding to aligned and random nanofibers at flow rates of 6, 9, 12 and 15 cm/s is presented in Figure 8(a).

Besides the increment in the flow rates affecting the pressure drop, it will also influence other properties, notably the filter efficiency. Thus, the outcome regarding the trend of particle capture efficiency at varying flow rates for the different fiber alignments under consideration has been studied in ANSYS Fluent, an established CFD software. Here, a computational domain having a velocity inlet, pressure outlet and symmetry sides, as earlier illustrated in Figure 1(e), was used for each of the domains and for each membrane. Also, fluid flow speeds of 0.1, 0.3, 0.5, 0.7 and 1 m/s were used. A discrete model was activated for every run and, in the discrete phase, the spherical drag law was applied for the flow of uniform anthracite particles having a diameter of 0.6 μm. For the size under consideration, the most significant force on the particles is the fluid drag; refer to Equations (17) and (18). The data generated from this analysis is presented in graph form in Figure 9.

Observations and discussion

Scanning electron microscopy analysis and fluid flow study. Firstly, from the scanning electron microscopy (SEM) images, it can be observed that none of the membranes had fibers aligning exclusively along a single direction, but rather, in both, there is some degree of randomness. However, there is a distinct difference in the way the fibers are aligned in both membranes (Figures 6(a) and (b)). It is on this basis that we refer to them as aligned and random nanofiber membranes. Regarding the porometry analysis, in both cases, several test runs were done and the relationship displayed in Figure 7(a) was consistent, that is, aligned membranes giving comparatively higher values of pressure. This is explained by the difference in pore sizes. Random nanofiber membranes possessed relatively larger pores compared with their aligned counterparts, where the largest pore through which there was a record of flow was 15.5 μm for random membranes and 7.617 μm for the aligned ones. In addition, Figure 7(c) shows that in aligned fiber webs, there is a higher number of smaller pores (<3 μm) contributing to flow compared to random webs (Figure 7(d)). For each

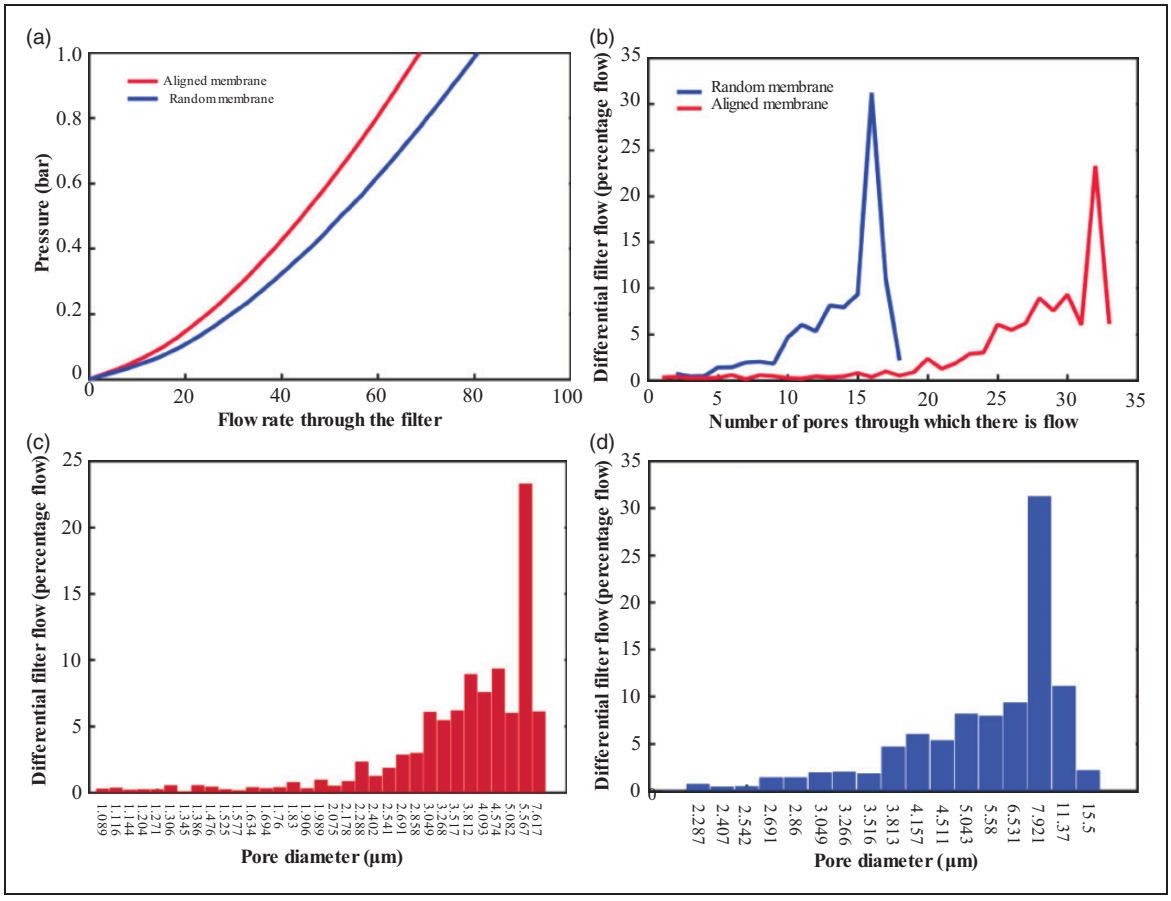

Figure 7. Using a capillary flow porometry machine, POROLUX™ 100, the rate of the flow of gas through the membrane and the resulting accrued pressure were plotted (a), then a plot of the differential filter flow resulting from the effect of the pore sizes in both random and aligned membranes was generated (b). Figures (c) and (d) give a representation of the percentage contribution to flow of nitrogen gas by each of the available pore sizes in aligned and random fiber membranes, respectively.

of the membranes, there is a modal (from mode) pore diameter that accounts for bulk of the flow through the medium. In the aligned fiber membrane, this was 5.56 μm diameter pores, accounting for 23.26% of the flow, while in random nanofiber membranes it was 7.921 μm diameter pores, accounting for 31.21% of the flow. It is clear that not only was the modal diameter in the random fibers larger, but also the percentage of flow for which it accounted was higher. From Figure 8, different approaches used to establish the contrast in performance between random and aligned fibers offer coincident trends in the results. It can be noted that the flow rate used in the experiment is relatively lower that what adopted for the model, which is because the flow rate in the testing equipment is often calibrated in line with that experienced during the course of usage. On the other hand, in the simulation procedure, higher velocities tend to be preferred for convenience. Another important factor in the pressure drop is the filter thickness and often times, we will adopt lesser thicknesses in the model than what is possible in an actual filter to make the model computationally manageable. This explains why even at low inlet velocities used for the electrospun membranes, the pressure is seen to be higher relative to what is obtained in the model. In addition, a perfect direct proportionality relationship is exhibited by the graphs generated with the data obtained from the model, unlike what is given by testing the actual membrane (Figure 8(a)). This can be explained by the fact that the Star CCM + software code calculates it pressure drop values in line with Darcy's law and, by strictly following this principle, a perfect direct proportionality relationship is set between the inlet velocity and pressure drop.

Capture efficiency and figure of merit. It is observed that increasing fluid flow velocity corresponded with an increase in the capture efficiency of particles. On the other hand, the FOM realized an equally steady fall in

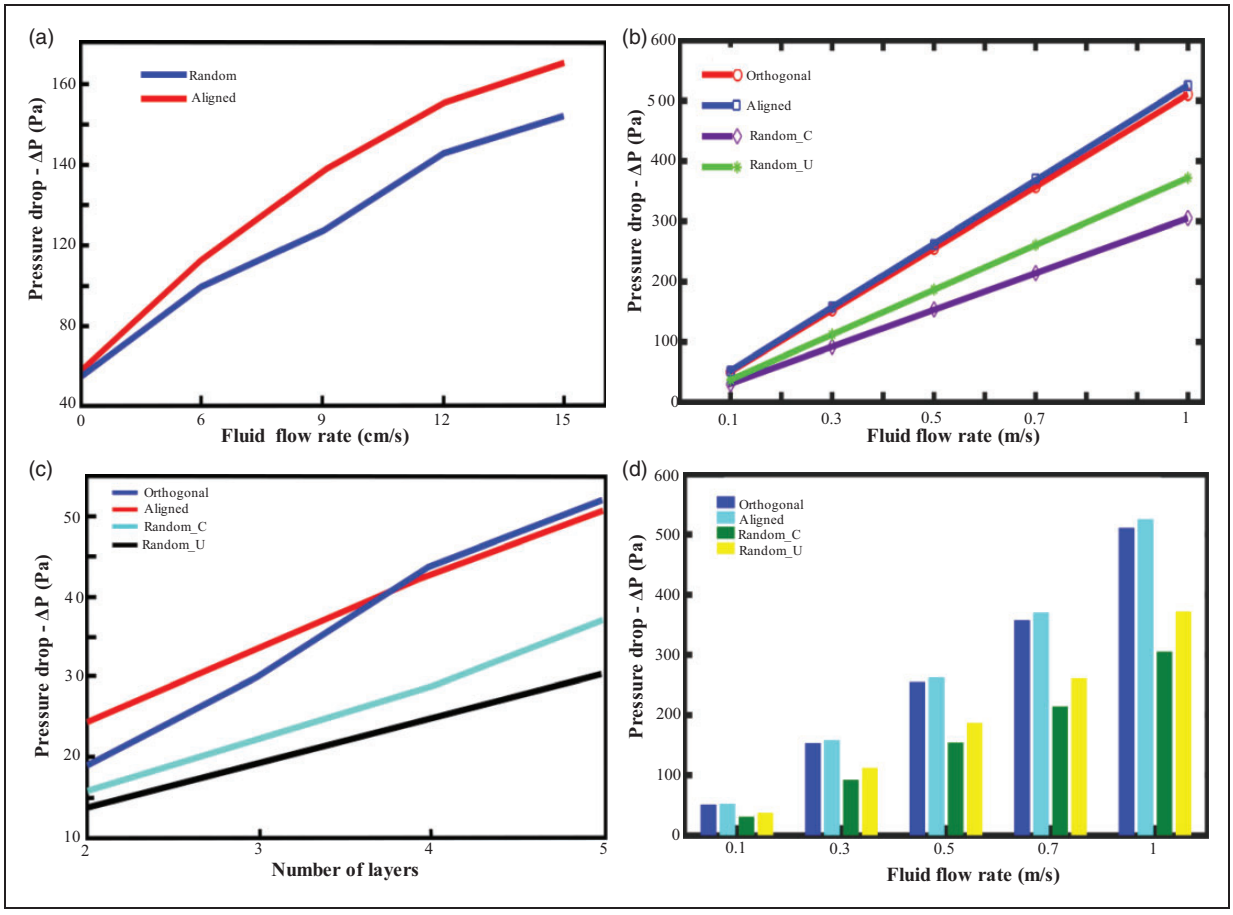

Figure 8. (a) Trend of pressure drop in both random and aligned membranes fabricated by the free surface electrospinning technique analyzed using an automatic filtration testing unit (Model 8130, TSI Group, USA). (b) Pressure drop in the virtual filter membranes with changing flow rates. (c) Similar to what we have in Figure 3(a), showing the pressure drop trend as the membranes increase in thickness at a constant flow rate, which has been imported here for comparison purposes. (d) Pressure drop in the membranes with increasing flow rate visualized in the form of bar plots.

value as the velocity was progressively increased. Starting with the steady rise achieved in capture efficiency, the 0.6 µm diameter particles used in this case are deposited onto the filter largely under the interception regime (Figure 9(c)). Particles within the interception regime possess a size that enables them to have a fairly low inertia so that during flow they will merely follow the fluid streamlines and if during their course of flow, their centers approach within a distance of $d_p/2$ of the collector surface, they will be deposited. This mechanism relies on the interception parameter R, given by

$$R = \frac{d_p}{d_f} \tag{21}$$

According to Ranz,[18] the equation for deposition by interception is given by

$$E_R = (1 + R) - \left(\frac{1}{1 + R}\right) \tag{22}$$

The reason for the increase in capture efficiency as the flow rate goes up is that whereas the particle inertia is low, at higher velocities it is still enough to deviate some of the particles from the fluid streamlines to deposit them by impaction. Meanwhile, whereas the capture efficiency registered a rise, the FOM, which is function of this together with the pressure drop, reduced steadily. Due to the inverse proportionality relationship existing between these two functions, the steady rise in filtration efficiency was countered by the sharp rise in pressure drop to give that kind of trend shown in the FOM plots. Overall, as manifested in Figures 8(b) and (d) as well as Figures 9(a) and (b), only a slight difference is observed in the performance between the two dissimilar random membranes as well as between the two dissimilar aligned fibers; however, what is profoundly clear is the difference in performance between what are generally random fiber and aligned fiber membranes.

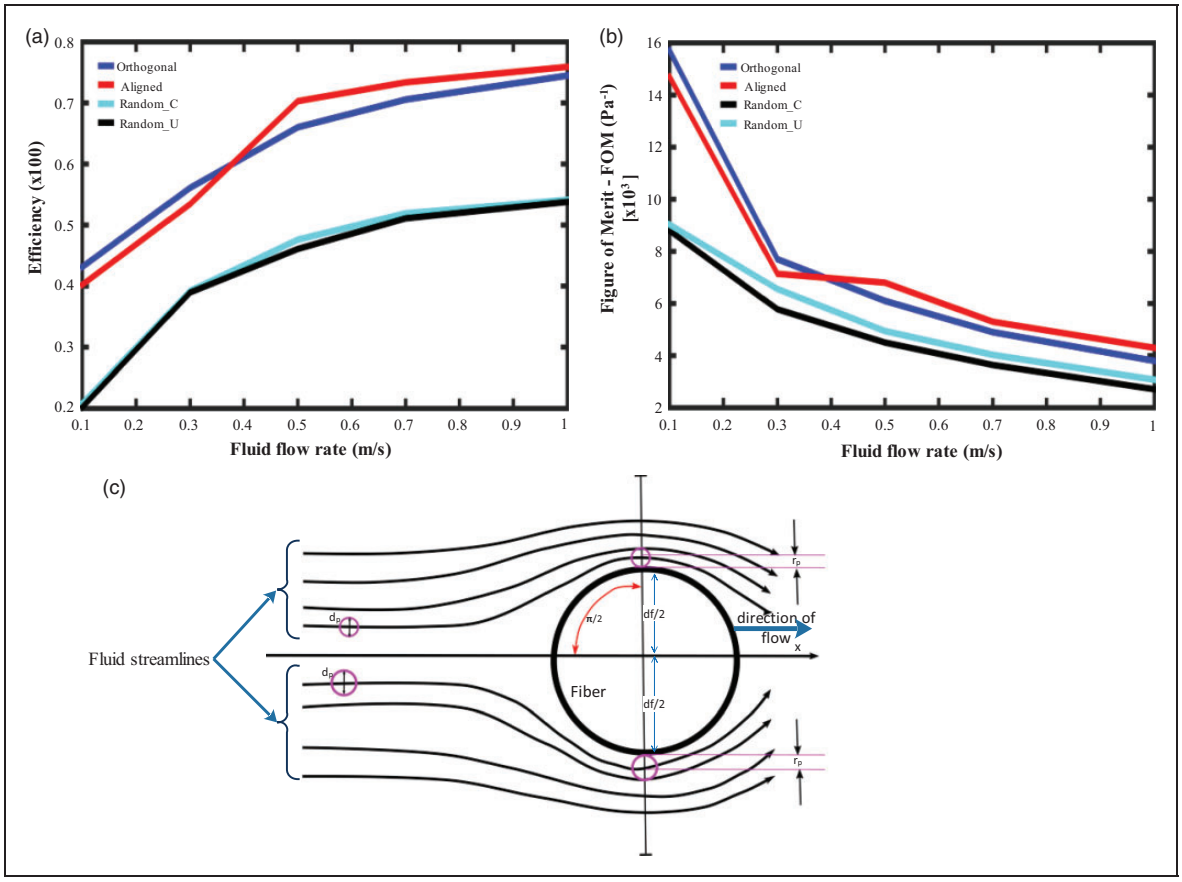

Figure 9. (a) Simulated particle capture efficiency as the fluid velocity at the inlet is progressively increased. (b) Figure of merit of the membranes as the velocity is increased. (c) Schematic of particle deposition in the interception regime.

Conclusion

Both the experimental and simulation results showed that pressure drop was higher in aligned fiber membranes as compared to their random counterparts, which agrees with some of the previous numerical work, for example the numerical method for predicting the flow permeability along and across random arrays presented by Sangani and Yao[19] shows that the random distribution of fibers in a membrane may increase its permeability by almost a factor of 2. Both the numerical study and capillary porometry analysis revealed that aligning nanofibers not only reduced the pore sizes but also increased the number of pores contributing to the fluid flow. Overall, the quality factor favors the aligned nanofiber membranes as the best.

Declaration of conflicting interests

The authors declared no potential conflicts of interest with respect to the research, authorship and/or publication of this article.

Funding

The authors disclosed receipt of the following financial support for the research, authorship and/or publication of this article: This work was partly supported by the Chang Jiang Youth Scholars Program of China and grants (51773037 and 51373033) from the National Natural Science Foundation of China to Prof. Xiaohong Qin as well as the 'Innovation Program of Shanghai Municipal Education Commission,' 'Fundamental Research Funds for the Central Universities' and 'DHU Distinguished Young Professor Program' to her. This work has also been supported by a grant (61771123) from the National Natural Science Foundation of China to Prof. Rongwu Wang and the Shanghai Sailing Program (18YF 1400400) to Dr Zhenzhen Quan.

ORCID iD

Xiaohong Qin https://orcid.org/0000-0003-4663-903X

References

1. Lamb H. *Hydrodynamics*, 6th edn, Euston Road, London: Cambridge University Press, 1932.
2. Spielman L and Goren SL. Model for predicting pressure drop and filtration efficiency in fibrous media. *Environ Sci Technol* 1968; 2: 279–287.
3. Tamada K and Fujikawa H. The steady two-dimensional flow of viscous fluid at low Reynolds numbers passing

through an infinite row of equal parallel circular cylinders. *Q J Mech Appl Math* 1957; 10: 425–432.
4. Darcy H. *Les fontaines publiques de la ville de Dijon: Exposition et application*. Batignolles, Paris: Victor Dalmont, 1856.
5. Miyagi T. Viscous flow at low Reynolds numbers past an infinite row of equal circular cylinders. *J Phys Soc Jpn* 1958; 13: 493–496.
6. Kuwabara S. The forces experienced by randomly distributed parallel circular cylinders or spheres in a viscous flow at small Reynolds numbers. *J Phys Soc Jpn* 1959; 14: 527–532.
7. Happel J. Viscous flow relative to arrays of cylinders. *AlChE J* 1959; 5: 174–177.
8. Chase GG, Swaminathan S and Raghavan B. Functional nanofibers for filtration applications. In: Wei Q (ed.) *Functional nanofibers and their applications*. Sawston, Cambridge: Woodhead Publishing, 2012, pp.121–152.
9. Kirsch AA and Fuchs N. Studies on fibrous aerosol filters—II. Pressure drops in systems of parallel cylinders. *Ann Occup Hyg* 1967; 10: 23–30.
10. Davies CN. The separation of airborne dust and particles. *Proc Inst Mech Eng Lond 1B* 1953; 167: 185–213.
11. Fuchs NA, Kirsch IB and Stechkina A. A contribution to the theory of fibrous aerosol filters. In: *Faraday symposia of the Chemical Society Symposium*, Swansea, 28–30 March 1973, paper no. 15, pp.143–156. Aberdeen: Royal Society of Chemistry.
12. Keller JB. Viscous flow through a grating or lattice of cylinders. *J Fluid Mech* 2006; 18: 94–96.
13. Tomadakis MM and Robertson TJ. Viscous permeability of random fiber structures: comparison of electrical and diffusional estimates with experimental and analytical results. *J Compos Mater* 2005; 39: 163–188.
14. Tahir M and Vahedi Tafreshi H. Influence of fiber orientation on the transverse permeability of fibrous media. *Phys Fluids* 2009; 21: 083604.
15. Cheng L, Rief S and Wiegmann A. Nano filtration media-challenges of modelling and computer simulation. *Filtech 2009 Proc* 2009; 2: 413–419.
16. Maxwell JC. On stress in rarefied gases arising from inequalities of temperature. *Philos Trans R Soc London* 1879; 170: 231.
17. McNenly MJ, Gallis MA and Boyd ID. Empirical slip and viscosity model performance for microscale gas flow. *Int J Numer Methods Fluids* 2005; 49: 1169–1191.
18. Ranz W. *The impaction of aerosol particles on cylindrical and spherical collectors*. University of Illinois, Urbana, Illinois, 1951.
19. Sangani AS and Yao C. Transport processes in random arrays of cylinders. II. Viscous flow. *Phys Fluids* 1988; 31: 2435–2444.

Nomenclature

Symbol Description

CFD computational fluid dynamics

SVF solid volume fraction of the filter membrane
d_p particle diameter (μm)
d_f fiber diameter (μm)
E efficiency of the filter medium
E_R particle deposition by the interception regime
F drag force per unit fiber length
F^* drag coefficient
h distance between two particles or a particle and a wall (μm)
k permeability of air through the filter
K_u Kuwabara's coefficient
N number of particles that are able to go through the filter medium
N_0 number of particles impacting the upstream side of the filter
P_1 pressure on the downstream side of the filter (Pa)
P_2 pressure on the upstream side of the filter (Pa)
P_n penetration of particles (of the particles originally directed at the filter medium, the portion that is able to go through)
u_f fluid velocity (m/s)
u_p particle velocity (m/s)
u_S fluid velocity relative to the moving particle_slip velocity (m/s)
U_0 superficial velocity (m/s)
v general velocity (m/s)
Z filter thickness (m or μm)

Mathematical operators and Greek letters

α the portion of the filter that is taken up by the fibers (SVF)
ϵ filter porosity
λ mean free path of the gas molecules or the average distance traveled by gas molecules between successive collisions; a value of 68 nm was assumed (m or nm)
μ dynamic viscosity of the fluid (m^2/s)
ρ_p particle density (kg/m^3)
τ_f characteristic time of the flow field (s)
τ_p time required for the particle to respond to change in fluid velocity (s)
ΔP pressure drop across a filter (Pa)
∇P pressure gradient (Pa/m)